

## Key Points:

- Comparison of zonal winds between the observed winds and computed winds validates a general thermal wind relationship
- A complete picture of zonal wind in Saturn's upper troposphere reveals that the equatorial zonal jets exhibit complex vertical structures
- Analysis over different years suggests that temporal-varying solar flux is one driving factor behind the seasonal changes in zonal winds

## Supporting Information:

Supporting Information may be found in the online version of this article.

## Correspondence to:

X. Wang,  
xwang216@CougarNet.UH.EDU










## Citation:

Wang, X., Li, L., Guan, L., Jiang, X., Fry, P. M., Dyudina, U. A., et al. (2025). Spatiotemporal variability of Saturn's zonal winds observed by Cassini. *Journal of Geophysical Research: Planets*, 130, e2024JE008515. <https://doi.org/10.1029/2024JE008515>

Received 22 MAY 2024

Accepted 2 JAN 2025

## Spatiotemporal Variability of Saturn's Zonal Winds Observed by Cassini

Xinyue Wang<sup>1</sup> , Liming Li<sup>2</sup> , Larry Guan<sup>2</sup>, Xun Jiang<sup>1</sup>, Patrick M. Fry<sup>3</sup> , Ulyana A. Dyudina<sup>4</sup>, Leigh N. Fletcher<sup>5</sup> , Enrique García-Melendo<sup>6</sup> , Ricardo Hueso<sup>7</sup> , Raúl Morales-Juberías<sup>8</sup> , Agustín Sánchez-Lavega<sup>7</sup> , and Amy A. Simon<sup>9</sup> 

<sup>1</sup>Department of Earth and Atmospheric Sciences, University of Houston, Houston, TX, USA, <sup>2</sup>Department of Physics, University of Houston, Houston, TX, USA, <sup>3</sup>Space Science and Engineering Center, University of Wisconsin-Madison, Madison, WI, USA, <sup>4</sup>Space Science Institute, Boulder, CO, USA, <sup>5</sup>School of Physics and Astronomy, University of Leicester, Leicester, UK, <sup>6</sup>Universitat Politècnica de Catalunya UPC, Terrasa, Spain, <sup>7</sup>Escuela de Ingeniería de Bilbao, Universidad del País Vasco, UPV/EHU, Bilbao, Spain, <sup>8</sup>Physics Department, New Mexico Institute of Mining and Technology, Socorro, NM, USA, <sup>9</sup>NASA Goddard Space Flight Center, Greenbelt, MD, USA

**Abstract** The strong zonal winds on giant planets are among the most interesting phenomena in our solar system. Observations recorded by the Composite Infrared Spectrometer (CIRS), the Imaging Science Subsystem (ISS), and the Visual and Infrared Mapping Spectrometer (VIMS) on the Cassini spacecraft are utilized to investigate spatiotemporal variations in Saturn's zonal winds. A general thermal wind equation works for investigating the vertical structure of zonal winds at all latitudes, but it has integration gaps near the equator caused by the cylindrical integration path. Here, we develop an algorithm to address this limitation, which is validated by the observed zonal winds. The algorithm is combined with the CIRS-retrieved temperature and the ISS-measured winds to generate a complete picture of the vertical structure of Saturn's zonal winds for the upper troposphere (i.e., 50–500 mbar), which suggests that the equatorial zonal winds have complicated vertical structures. The zonal winds from 10°S to 10°N initially decrease with altitude and then increase. Additionally, the intense narrow equatorial jet between 3°S and 3°N widens with altitude. The zonal winds are further used to examine the atmospheric stability, which implies some unstable regions. Finally, the analysis of Cassini multi-instrument observations reveals different temporal behaviors of zonal winds in the vertical direction, which suggests that seasonally varying solar flux is one of the drivers of temporal variations in zonal winds.

**Plain Language Summary** Strong atmospheric currents in the longitudinal direction (i.e., zonal winds) on giant planets are among the interesting phenomena in our solar system. Long-term multi-instrument observations recorded by the Cassini spacecraft are combined with a general thermal wind equation to investigate spatiotemporal variations in Saturn's zonal winds. The complete picture of the vertical structure of Saturn's zonal winds indicates that equatorial zonal winds in the upper troposphere (i.e., 50–500 mbar) initially decrease with altitude and then increase. The stability investigation suggests some unstable regions in the upper troposphere. The different temporal behaviors of zonal winds in the vertical direction reveal that seasonally varying solar flux also plays a critical role in temporal variations in Saturn's zonal winds.

## 1. Introduction

The atmospheres of all giant planets in our solar system exhibit dominant atmospheric currents in the longitudinal direction. These large-scale currents, known as zonal winds, can be measured by averaging the winds longitudinally over large areas. Saturn's zonal winds can reach speeds of approximately 400 m/s at the pressure levels of visible clouds, significantly stronger than the strongest large-scale winds on Earth (~100 m/s). Such strong zonal winds play critical roles in the atmospheric dynamics of the ringed planet (e.g., Del Genio et al., 2009; Ingersoll, 2020).

The Cassini data sets of Saturn, collected over approximately 13 years from Saturn's northern winter (2004–2009) to northern spring (2009–2017), provide a unique opportunity to explore the seasonal variability of the planet's zonal winds. Additionally, different scientific instruments on Cassini probe different pressure levels in Saturn's atmosphere, allowing us to investigate the vertical structure of its zonal winds. In this study, we primarily use observations recorded by the Imaging Science Subsystem (ISS) and the Composite Infrared Spectrometer (CIRS) to explore the spatiotemporal variability of Saturn's zonal winds in the upper troposphere. Here, Saturn's upper

troposphere is defined as the upper portion of the troposphere from the pressure level of the top visible clouds at approximately 500 mbar to the tropopause around 50 mbar. Additionally, observations conducted by the Visual and Infrared Mapping Spectrometer (VIMS) are used to explore the zonal winds at relatively deeper atmospheric layers. Many studies of Saturn's zonal winds based on Cassini observations exist (e.g., see review by Ingersoll, 2020), but a systematic analysis of the spatiotemporal variability of Saturn's global zonal winds, by combining data from the three Cassini instruments (ISS, CIRS, and VIMS), is still lacking.

The images recorded by the multiple filters (i.e., wavelengths) of the ISS can be used to measure zonal winds at different pressure levels. In particular, images recorded by the ISS continuum filters can be used to track features of the top visible clouds ( $\text{NH}_3$ ) around 500 mbar and thereby measure the zonal winds at that level (e.g., Del Genio et al., 2009; García-Melendo et al., 2010, 2011; Li et al., 2011; Porco et al., 2005; Sayanagi et al., 2013; Sanchez-Lavega et al., 2016; Vasavada et al., 2006). Furthermore, the ISS-measured zonal winds at 500 mbar can serve as a lower boundary condition for the thermal wind equation. When these winds are coupled with the CIRS-retrieved temperature through the thermal wind equation, the vertical structure of zonal winds above the reference level (i.e., 500 mbar) can be derived (e.g., Flasar, Achterberg, Conrath, Gierasch, et al., 2005; Flasar, Achterberg, Conrath, Pearl, et al., 2005b; Fletcher et al., 2016, 2017; Li et al., 2008, 2011). Rather than employing the classic thermal wind equation, we utilize a general thermal wind equation (see Section 3). In principle, the general thermal wind equation can be used for all latitudes because it does not depend on geostrophic balance. In practice, the equation still has a gap in the equatorial region due to its cylindrical integration path (see Figure 1 in the Section 3), preventing us from examining the zonal winds within the gap. We develop an algorithm to address the integration gap so that a complete picture of global zonal winds can be examined. In addition to the ISS and CIRS observations, Cassini VIMS observations were also analyzed. The VIMS 5- $\mu\text{m}$  images sense the atmospheric layers around 2,000 mbar (i.e., Baines et al., 2005; Choi et al., 2009; Fletcher, Baines, et al., 2011; Momary et al., 2006), which are below the atmospheric layers probed by the ISS and CIRS. Therefore, the VIMS 5- $\mu\text{m}$  images provide a unique opportunity to examine Saturn's zonal winds in relatively deep atmospheric layers. A systematic analysis of Saturn's zonal winds also makes it possible to explore other dynamics of this ringed planet.

Saturn's rotation period, serving as the reference for measuring zonal winds, has been investigated for a long time (e.g., Anderson & Schubert, 2007; Desch & Kaiser, 1981; Giampieri et al., 2006; Helled et al., 2009, 2015; Mankovich et al., 2019; Militzer & Hubbard, 2023; Read, Dowling, & Schubert, 2009). A recent review (Sanchez-Lavega et al., 2023) includes a good summary of the discussion of different rotation periods suggested for Saturn. In this study, we adopt system III Saturn rotation period (i.e., 10 hr, 39 min, and 22 s) (Desch & Kaiser, 1981) suggested by the International Astronomical Union (Archinal et al., 2018). This choice aims to facilitate the comparison of zonal winds between this work and previous studies because most previous studies used such a system. The conversion of zonal winds from system III to other systems, which is straightforward, is not included.

## 2. Cassini Data Sets and Data Processing

Our wind measurements rely on data recorded by three instruments aboard Cassini: ISS, VIMS, and CIRS. The data sets recorded by the three instruments and analyzed in this study are summarized in Table S1 of the Supporting Information S1. Here, we briefly introduce each instrument and its corresponding data sets and data processing methods.

The ISS instrument (Porco et al., 2004) is a two-dimensional multi-spectral imaging device on Cassini. Previous studies (e.g., Li et al., 2004, 2006a, 2011) have detailed the use of ISS images and image processing techniques for measuring zonal winds. Basic image processing involves navigation, photometric calibration, and map projection based on the camera's geometric model and the photometric calibration software (CISSCAL) (Porco et al., 2004), in addition to data from the Navigation and Ancillary Information Facility (NAIF) at the Jet Propulsion Laboratory (Vasavada et al., 2006). Processed ISS multi-filter maps facilitate the measurement of zonal winds around two pressure levels (e.g., Del Genio et al., 2009; García-Melendo et al., 2010, 2011; Li et al., 2011; Porco et al., 2005; Sayanagi et al., 2013; Sánchez-Lavega et al., 2016). Maps derived from ISS images recorded with middle and strong methane-absorption filters (MT2 and MT3) are utilized for measuring zonal winds around the 60-mbar pressure level (e.g., García-Melendo et al., 2010, 2011; Sanchez-Lavega et al., 2016) near Saturn's tropopause (i.e., 50 mbar). Additionally, maps from ISS images recorded with three continuum filters (CB1, CB2,

and CB3) are employed to measure zonal winds around the pressure level of the top visible clouds ( $\text{NH}_3$ ) at  $\sim 500$  mbar (e.g., García-Melendo et al., 2010, 2011; Sanchez-Lavega et al., 2000, 2016).

The CIRS instrument, a Fourier-transform spectrometer (Flasar et al., 2004), plays a crucial role in determining the thermal structure and chemical components of Saturn's atmosphere. Spectra from CIRS observations allow for the retrieval of Saturn's atmospheric temperature at different pressure levels. The retrieval scheme for atmospheric temperature from infrared spectra is detailed by Conrath and Gautier (1980) and Conrath et al. (1998). CIRS observations provide limited information in the pressure range of 5–50 mbar and at pressures greater than approximately 500 mbar (Flasar et al., 2004; Fletcher et al., 2007). Zonal-mean atmospheric temperature between 50 and 500 mbar in Saturn's troposphere was retrieved from CIRS high-spatial-resolution nadir radiance in a previous study (Fletcher et al., 2018), which is directly used in this study (see Table S1 in Supporting Information S1 for more information).

The Cassini ISS and CIRS observations can be combined with the thermal wind equation to examine the zonal winds from 50 to 500 mbar. Additionally, the Cassini VIMS observations allow exploration of zonal winds at deeper layers. VIMS, a mapping spectrometer, captures images at 352 different wavelengths between 0.35 and 5.1  $\mu\text{m}$  (Brown et al., 2004). The standard VIMS data processing pipeline, developed by the VIMS team, includes procedures such as cosmic ray hit removal and flat field calibration (McCord et al., 2004; Sromovsky & Fry, 2010), with further data reduction and processing utilizing the Integrated Software for Imagers and Spectrometers (ISIS) (Gaddis et al., 1997). VIMS 5- $\mu\text{m}$  images probe Saturn's atmosphere at pressure levels around 2,000 mbar (Baines et al., 2005, 2009; Choi et al., 2009; Fletcher, Baines, et al., 2011; Momary et al., 2006), deeper than those probed by Cassini ISS and CIRS. While some previous studies have examined VIMS 5- $\mu\text{m}$  observations (Baines et al., 2005, 2009; Choi et al., 2009; Momary et al., 2006; Studwell et al., 2018), research on temporal variations of relatively deep zonal winds, particularly in the equatorial region, remains limited.

It should be noted that precisely determining the pressure levels sensed by the ISS and VIMS observations is challenging due to various factors, such as the optical and spatial characteristics of aerosols and cloud particles, as well as the types and vertical extensions of clouds. Previous investigations (e.g., García-Melendo et al., 2010, 2011; Sanchez-Lavega et al., 2000, 2016) suggest that the uncertainty in estimating the pressure levels of the top clouds sensed by the ISS continuum filters can be as high as  $\sim 150$  mbar. On the other hand, the estimated pressure levels for the cloud features observed in the VIMS 5- $\mu\text{m}$  images have an uncertainty of  $\sim 1,000$  mbar (e.g., Baines et al., 2005; Choi et al., 2009; Fletcher, Baines, et al., 2011; Momary et al., 2006). These uncertainties in the pressure levels of cloud features are considered in our subsequent investigations of zonal winds.

### 3. Methodology of Zonal-Wind Measurements

Clouds captured in the ISS and VIMS images can serve as tracking features for measuring zonal winds. There are two methods for cloud tracking: manual tracking and automatic correlating. Manual tracking involves observing cloud movements in images taken at different times and translating these movements into zonal winds. Alternatively, Limaye (1986) developed a computer algorithm, known as automatic correlating, to track cloud features in images. This method entails extracting east-west strips of pixels from image pairs, shifting them to identify the maximal cross-correlation coefficient, and calculating zonal winds based on the lags in the longitude direction with the maximal cross-correlation coefficient. This technique has been employed in numerous previous studies using Cassini ISS and VIMS images (e.g., Baines et al., 2009; Choi et al., 2009; García-Melendo et al., 2010, 2011; Li et al., 2004, 2006a, 2006b, 2011; Sayanagi et al., 2013; Sánchez-Lavega et al., 2016; Studwell et al., 2018). It is worth noting that these two methods, manual tracking and automatic correlating, are not mutually exclusive. Instead, they are commonly used in combination to explore zonal winds in planetary atmospheres.

Another method for exploring Saturn's zonal winds involves utilizing the CIRS-retrieved temperature data in conjunction with the thermal wind equation. The thermal wind equation (Batchelor, 1967; Pedlosky, 1987) relates vertical wind shear to the meridional temperature gradient along isobaric surfaces, making it a valuable tool for investigating the vertical structure of zonal winds in atmospheric and planetary sciences. The meridional gradient in molecular weight associated with gas condensation can also affect the wind field (e.g., Sun et al., 1991; Tollefson et al., 2021), but it does not significantly affect Saturn's wind field because the concentrations of condensable gases in the ringed planet are very small.

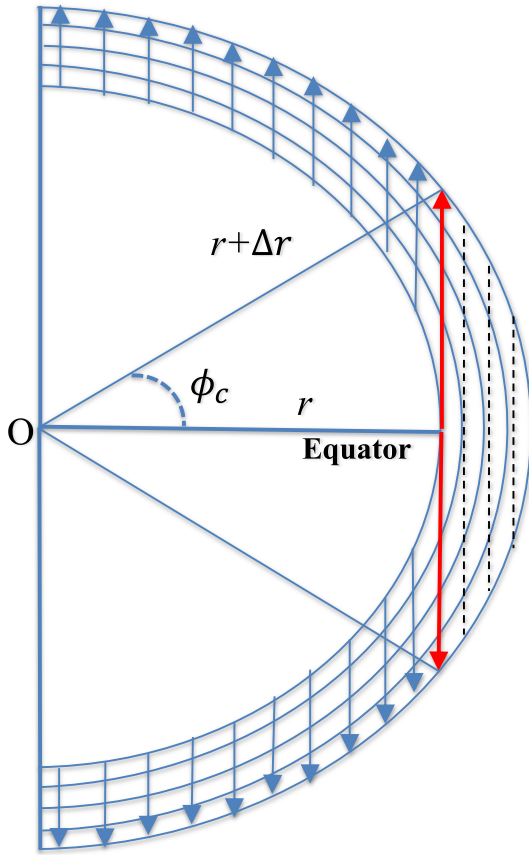


**Figure 1.** Cylindrical integration paths were used in our thermal wind equation. The radius from the center of a planet to the reference level is defined as  $r$ . The total thickness of all atmospheric layers which we are interested in is defined as  $\Delta r$ . For the upward integration, the latitude at the top layer reached by the cylindrical integration path originating from the equator at the reference level is defined as  $\phi_c$ .

The classical thermal wind equation, formulated in Cartesian coordinates under the assumption of geostrophic balance, becomes ineffective at low latitudes where geostrophic balance breaks down near the equator. In recent years, a general equation linking the temperature field to the wind field has been developed, employing either cylindrical or spherical coordinates (e.g., de la Torre Juarez et al., 2002; Flasar, Achterberg, Conrath, Gierasch, et al., 2005; Flasar, Achterberg, Conrath, Pearl, et al., 2005b; Fletcher et al., 2017; Fouchet et al., 2008; Galanti et al., 2017; Li et al., 2007, 2008; Marcus et al., 2019). Unlike the classical equation, this generalized thermal wind equation does not rely on geostrophic balance, rendering it applicable across all latitudes, including the equatorial region. For Saturn, characterized by a robust equatorial jet exceeding 400 m/s, the term associated with centrifugal force should be considered. Therefore, the gradient-wind balance instead of geostrophic balance is employed in the relationship between temperature and wind fields (e.g., Flasar, Achterberg, Conrath, Gierasch, et al., 2005; Flasar, Achterberg, Conrath, Pearl, et al., 2005b; Fouchet et al., 2008; Li et al., 2007, 2008), which can be expressed in cylindrical coordinates as

$$\frac{\partial}{\partial z} \left| \left( \frac{u^2 + 2\Omega u r_c}{r_c} \right) \right| = \frac{R}{pr} \frac{\partial p}{\partial r} \frac{\partial T}{\partial \phi} \Big|_p \quad (1)$$

where  $z$  is a unit vector along the rotation axis,  $r_c$  is the cylindrical radius,  $u$  is zonal winds,  $\Omega$  is the angular speed of rotation of a planet,  $R$  is the specific gas constant,  $p$  is pressure,  $r$  is the radius of the planet,  $T$  is temperature, and  $\phi$  is planetocentric latitude (see Figure 1). The derivation process of Equation 1 is presented in Supporting Information S1.

We integrate the term containing the temperature gradient on the right-hand side of Equation 1 along the cylindrical path to derive the term involving the zonal winds on the left-hand side and then solve for the zonal winds. In this process, we conduct upward integration along the cylindrical path from a reference pressure level (500 mbar), where zonal winds are measured using ISS images captured by the continuum filters. The temperature gradient on the

right-hand side is computed based on the temperature retrieved by CIRS. The CIRS temperature retrieved at constant pressure levels lies on the oblate surfaces of Saturn due to its oblate shape. The difference in latitude differential  $\partial\phi$  between oblate surfaces and spheric surfaces is typically  $\sim 2\%$  of the latitude differential, which is neglected in our calculation. The conversion from spherical coordinates to cylindrical coordinates should also be considered when applying Equation 1. While converting between the two coordinate systems is relatively straightforward for middle and high latitudes, it requires more attention at low latitudes due to the significant increase in latitude excursion near the equator.

During the upward integration of Equation 1, the cylindrical path originating from the equator at the reference level (i.e., 500 mbar) goes up to the top of the investigated atmospheric layers at 50 mbar. This integration process is depicted by the red arrows in Figure 1. For the atmospheric region to the right of the red arrows, there are no upward cylindrical integration paths originating from the reference level. Hence, our cylindrical thermal wind equation is not applicable in this region. To estimate the extent of this region, we define the latitude at the top layer reached by the cylindrical integration path originating from the equator as  $\phi_c$  (see Figure 1). For a spherical body, we have  $\phi_c = \arccos[r/(r + \Delta r)]$ , where  $r$  and  $\Delta r$  represent Saturn's radius at the reference level and the total thickness of the investigated atmospheric layers, respectively. Therefore, the thickness of the investigated atmospheric layers determines the latitude  $\phi_c$ , a parameter representing the integration gaps around the equator. The atmospheric layers from 500 to 50 mbar, investigated by ISS/CIRS, have a total thickness  $\Delta r \sim 100$  km. Saturn's equatorial radius at the reference level (500 mbar) is  $r \sim 60,308$  km, which is the sum of the thickness from 1,000 mbar to the reference level (40 km) and the equatorial radius at 1,000 mbar (60,268 km) (Archinal et al., 2018). Therefore, we have  $\phi_c \sim 3.3^\circ$ .

Now, we explain how to address the gaps in the integration paths of the cylindrical thermal wind equation (i.e., the region to the right of the red arrows in Figure 1). Although the latitude excursion from the equator at the reference level (500 mbar) to the top of the relevant atmosphere (50 mbar) can reach  $3.3^\circ$  along the cylindrical path, the latitude excursions between neighboring atmospheric layers are much smaller than  $3.3^\circ$  because Saturn's temperature was retrieved for 18 layers of the atmosphere between 500 and 50 mbar (Fletcher et al., 2017). For instance, the latitude excursion from the equator at the reference level (500 mbar) to the nearest level below (440 mbar) is approximately  $\sim 0.9^\circ$ . We designate the level closest to the reference level as the first level, with subsequent levels following this sequence (i.e., the second level, the third level, and so forth). For each level, the temperature retrieved by CIRS was mapped onto a regular latitude grid with a latitudinal resolution of  $1^\circ$  (Fletcher et al., 2017).

The latitude excursion from the reference level to the first level ( $\sim 0.9^\circ$ ) implies that the zonal wind at the equator (latitude  $0^\circ$ ) at the reference level generates zonal winds at latitudes  $0.9^\circ$  ( $0.9^\circ\text{N}$  and  $0.9^\circ\text{S}$ ) at the first level through cylindrical integration of the thermal wind equation. Subsequently, we linearly interpolated the calculated first-level zonal winds at  $0.9^\circ\text{N}$  and  $0.9^\circ\text{S}$  to obtain zonal winds at the equator. This method enables us to fill the equatorial gap for the first level. Zonal winds at regular latitude grids other than the equator (e.g.,  $1^\circ$ ,  $2^\circ$ ,  $3^\circ$ , etc.) at the reference level are also integrated vertically to irregular latitudes at the first level due to the latitude excursion caused by cylindrical integration. Similarly, we can linearly interpolate zonal winds at irregular latitudes to zonal winds at regular latitudes at the first level. After obtaining zonal winds at all regular latitudes at the first level, we designate the first level as a new reference level and apply the cylindrical thermal wind equation from this new reference level to the next level. This iterative process continues to the top level, allowing us to obtain zonal winds at regular latitudes for all levels.

Although the above method effectively fills observational gaps in the equatorial region, computing Saturn's equatorial zonal winds is an additional challenge. Analyses based on Cassini/ISS observations (García-Melendo et al., 2010) revealed fine structures of zonal winds at latitudinal scales of less than  $1^\circ$  in Saturn's equatorial region. Therefore, linear interpolation of Saturn's zonal winds from irregular latitudes to regular latitudes introduces significant uncertainty when the latitude excursion is close to  $1^\circ$  (e.g.,  $0.9^\circ$  for the latitude excursion from the reference level to the first level) because linear interpolation cannot resolve fine structures. To address this issue, we try two approaches: (a) We linearly interpolate ISS zonal winds at the reference level and CIRS temperatures from relatively coarse latitudinal resolutions to finer resolutions, and (b) we linearly interpolate CIRS temperatures to additional pressure levels in the vertical direction. Such interpolations make the conversion of zonal winds from irregular to regular latitudes more accurate, allowing the fine structure of equatorial zonal winds to be resolved. Our tests suggest that the interpolation of spatial resolution is more effective in the latitudinal direction than in the vertical direction. A meridional resolution of  $0.2^\circ$  or better can resolve the fine structure of equatorial winds as revealed by the Cassini/ISS observations. In this study, we linearly interpolated the CIRS-retrieved temperature from the original  $1^\circ$  to  $0.1^\circ$  in the meridional direction to resolve the fine structures of equatorial winds. Correspondingly, we linearly interpolate the ISS winds, which serve as the boundary condition for the integration of the thermal wind equation, from a spatial resolution of  $0.2\text{--}0.3^\circ$  to  $0.1^\circ$  in the meridional direction. In the vertical direction, we linearly interpolate the pressure levels of the CIRS-retrieved temperature from the original 18 vertical layers between 500 and 50 mbar to 90 levels.

Uncertainties in wind measurements are crucial for understanding spatiotemporal variations of Saturn's zonal winds. For zonal winds measured by cloud-tracking techniques with ISS and VIMS images, systematic errors caused by changes in clouds, wave-like phenomena, and interactions between clouds and their environment introduce uncertainties in zonal wind measurements (García-Melendo & Sanchez-Lavega, 2001; Li et al., 2004). We estimate uncertainties in cloud-tracking zonal winds by the standard deviation of multiple wind measurements within each latitude bin. Additionally, uncertainty related to ISS/VIMS image navigation procedures is also considered in our estimation of zonal wind measurement uncertainties.

For uncertainties in computed zonal winds from the thermal wind equation with CIRS-retrieved temperatures, three main sources of uncertainty exist: (1) uncertainty in measurements of the speed of cloud-tracking zonal winds at 500 mbar, used as boundary conditions for the thermal wind equation; (2) uncertainty in determining the pressure level of zonal winds in the reference level at 500 mbar; and (3) uncertainty in CIRS-retrieved temperatures, which influences the temperature gradient and consequently affects integration of the thermal wind



equation. For the uncertainty source (1), zonal winds at 500 mbar are from a previous study (García-Melendo et al., 2011), which used Cassini images recorded at continuum filters for measurements. The uncertainty in the speed measurements of 500-mbar zonal winds ( $\sim 10$  m/s) (see García-Melendo et al., 2011) at the boundary is propagated to each pressure level above the boundary and remains constant during upward integration.

As suggested in previous investigations (e.g., Flasar, Achterberg, Conrath, Gierasch, et al., 2005; Flasar, Achterberg, Conrath, Pearl, et al., 2005b; García-Melendo et al., 2011; Sanchez-Lavega et al., 2000, 2016), the uncertainty in estimating the pressure level of zonal winds around 500 mbar can reach  $\sim 150$  mbar. A previous study (Li et al., 2013) examined this uncertainty in computing zonal winds using the thermal wind equation and suggested a magnitude of  $\sim 20$  m/s for this uncertainty. The computed zonal winds at different pressure levels (see Figure 2 in the next section), which are from the thermal wind equation, can also be used to investigate such an uncertainty. We compare the zonal winds between 350 and 500 mbar to estimate the uncertainty in computed zonal winds related to the uncertainty in the pressure levels of cloud features. Figure S1 in Supporting Information S1 suggests that there is no significant vertical shear of zonal winds between these two pressure levels, except for the narrow latitude band around the equator. The magnitude of the difference in equatorial zonal winds between the two pressure levels (i.e., 350 and 500 mbar) is  $\sim 20$  m/s, which is consistent with previous studies (Li et al., 2013). Here, we use the difference in zonal winds between the pressure levels, which is presented in Figure S1 in Supporting Information S1, to estimate the uncertainty in computed zonal winds caused by the uncertainty source (2).

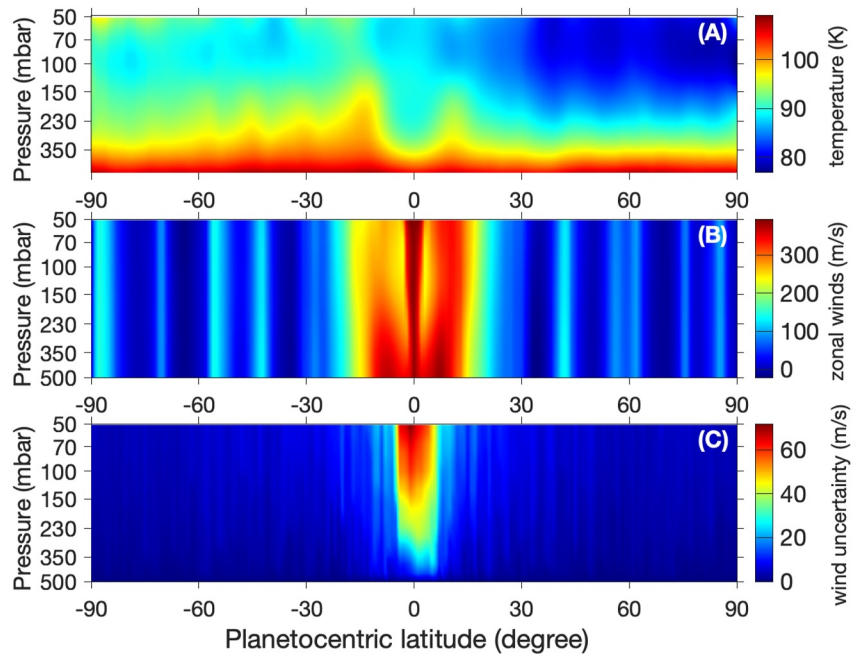
To estimate the uncertainty of computed zonal winds caused by errors in retrieved temperatures (i.e., uncertainty source (3)), we must examine the uncertainty of retrieved temperatures. The estimated uncertainty of CIRS-retrieved temperatures is 2–4 K, depending on the pressure level (Fletcher et al., 2017). Here, we use 3 K for uncertainty. We generate temperature uncertainty using random numbers with a magnitude of 3 K. Assuming that temperature uncertainty is independent of latitudinal direction and applying the rule of error propagation of addition (Bevington & Robinson, 2003), we use uncertainties at two neighboring latitudes to estimate uncertainty of temperature difference ( $\partial T$ ) in Equation 1. Likewise, assuming that temperature uncertainty is independent in the vertical direction, we can approximate vertical integration in Equation 1 using rule of error propagation of addition. This approach allows us to compute the uncertainty of computed zonal winds at every pressure level. It's worth noting that uncertainty of computed zonal winds from errors of retrieved temperature accumulates during upward integration.

## 4. Results

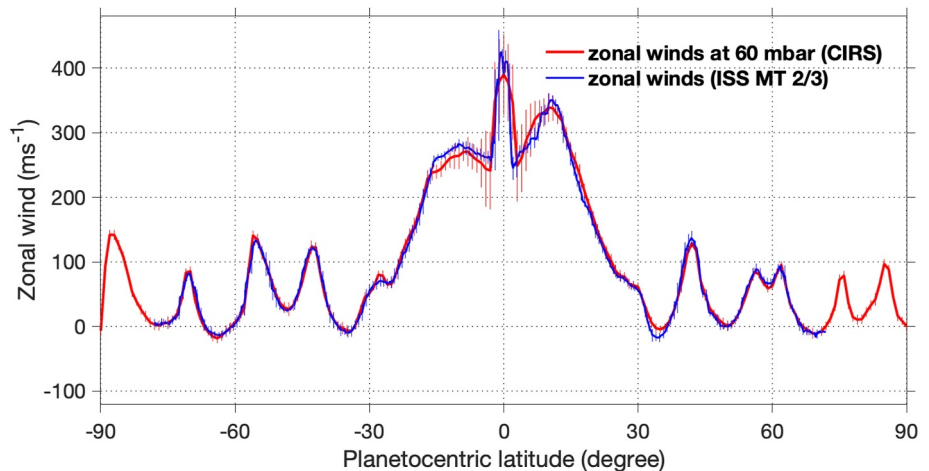
### 4.1. Vertical Structure of Zonal Winds

Figure 2 illustrates the CIRS-retrieved temperature (Figure 2a) and the corresponding computed zonal winds for the atmospheric layers from 500 to 50 mbar (Figure 2b), including the estimated uncertainties (Figure 2c). The cloud-tracking zonal winds at 500 mbar, obtained from a previous study based on images recorded by the ISS continuum filters (García-Melendo et al., 2011), are used as the boundary condition for the thermal wind equation. The zonal winds from the previous study represent time-averaged measurements over the period of 2004–2009. Therefore, to maintain consistency, we averaged the CIRS-retrieved temperature from the same previous study (Fletcher et al., 2017) over the same period (2004–2009), as shown in panel A of Figure 2.

Panel B of Figure 2 indicates that zonal winds essentially remain constant in the vertical direction in the middle and high latitudes, consistent with previous studies (e.g., Fletcher et al., 2016; Read, Conrath, et al., 2009). In the equatorial region, the zonal winds exhibit significant vertical variations. Initially, the equatorial winds between  $10^\circ\text{S}$  and  $10^\circ\text{N}$  decrease with altitude and then begin to increase. Furthermore, the pressure level at which this change from decrease to increase occurs varies with latitude. For the intense narrow equatorial jet between  $3^\circ\text{S}$  and  $3^\circ\text{N}$ , it extends throughout the entire pressure range of 50–500 mbar and widens with altitude. The thermal-wind equations suggest that the vertical shear of zonal winds is proportional to the meridional gradient of temperature; therefore, the relatively large meridional gradients of Saturn's temperature in the equatorial region contribute to the significant vertical variations of zonal winds there. Additionally, the thermal-wind equation implies that the vertical shear of zonal winds is proportional to the inverse of the Coriolis parameter. The Coriolis parameter strongly decreases from the high/middle latitudes to the equator, resulting in a dramatic increase in the vertical shear of zonal winds with decreasing latitude.



**Figure 2.** Saturn's CIRS-retrieved temperature and computed zonal winds for the upper troposphere (50–500 mbar). (a) A cross-section of latitude and pressure displaying the CIRS-retrieved temperature averaged over the period of 2004–2009. (b) Vertical structure of zonal winds. The zonal winds in panel (b) were computed by vertically integrating the thermal wind equation using zonal winds at the reference level at ~500 mbar. The zonal winds at the 500-mbar level are measured by the ISS images recorded at the continuum filters (CB2 and CB3) (García-Melendo et al., 2011). (c) Uncertainty of computed zonal winds. The estimate of uncertainty is primarily based on the retrieval errors of CIRS temperature by applying error propagation through the thermal wind equation.



**Figure 3.** Comparison of Saturn's 60-mbar zonal winds between the computed results based on the CIRS-retrieved temperature (red line) and the ISS measurements (blue line). The ISS images recorded by MT2 and MT3 filters were used to measure the zonal winds at ~60 mbar (García-Melendo et al., 2011), and the CIRS-derived winds at 60 mbar come from the results shown in Figure 2 (panel b).

To validate the vertical structure of zonal winds computed by the general thermal-wind equation with the CIRS temperature, we compare the computed zonal winds at the pressure level with the cloud-tracking measurements based on the ISS images. The ISS images recorded at the MT2 and MT3 filters have been used to measure the zonal winds at the pressure levels around 60 mbar (García-Melendo et al., 2011), which are compared with the CIRS-computed zonal winds at the same pressure level. The comparison, as shown in Figure 3, suggests basic

consistency of zonal winds between the two results at middle and high latitudes. A discrepancy in zonal winds between the two results primarily appears in the tropical region, even though the computed zonal winds from the CIRS-retrieved temperature captured the dominant structures of Saturn's equatorial jets around the tropopause (e.g., the narrow and strong eastward jet between 3°S and 3°N). However, this discrepancy is generally smaller than the uncertainty associated with zonal wind measurements, indicating that the two results for determining zonal winds are statistically consistent. It should be noted that the uncertainty in estimating the pressure levels of features presented in the ISS images recorded by MT2/3 filters (e.g., García-Melendo et al., 2011) is not considered in the uncertainty of the cloud-tracking zonal winds. Such uncertainty may also contribute to the discrepancy between the CIRS-computed and ISS-tracked zonal winds.

Figure 2 uses the zonal winds around 500 mbar, measured by the ISS images recorded with the CB2 and CB3 filters, as the boundary condition and integrates Equation 1 upward to obtain the zonal winds between 50 and 500 mbar. The zonal winds around 60 mbar, which are measured by the images recorded with the MT2 and MT3 filters, can be also served as the boundary condition. With such a boundary condition, we can integrate Equation 1 upward to 50 mbar and downward to 500 mbar to obtain the zonal winds for the pressure range of 50–500 mbar. The comparison of the 500-mbar zonal winds between the measurements based on ISS CB2/3 images and the computed results from the downward integration using CIRS temperature data, presented in Figure S2 of the Supporting Information S1, suggests consistency between the two results within the uncertainties. This indicates that integrating the thermal wind relationship with the ISS MT2/3 winds at 60 mbar as the boundary condition is also effective in exploring the vertical structure of Saturn's zonal winds. Figure S3 in Supporting Information S1 further compares the zonal winds from the two integrations with different boundary conditions, showing that both integrations reveal a generally consistent vertical structure of zonal winds.

There are many more wind measurements of 500-mbar zonal winds based on ISS CB2/3 images compared to the 60-mbar zonal winds based on ISS MT2/3 images, making the 500-mbar zonal winds more robust with relatively smaller uncertainties. Therefore, using the 500-mbar zonal winds as the boundary condition for the thermal wind integration, as discussed in the main text, is preferred.

#### 4.2. Atmospheric Stabilities Based on the Spatial Variations of Zonal Winds

The vertical structure of zonal winds displayed in panel B of Figure 2 enables further exploration of Saturn's atmospheric dynamics. We first examine the static stability of Saturn's upper troposphere based on the CIRS-retrieved temperature (panel A of Figure 2) computing the Brunt-Väisälä frequency  $N^2 = (g/\theta)(d\theta/dz)$ , where  $g$  is gravity,  $\theta$  is the potential temperature, and  $z$  is height. Then the static stability is combined with the vertical shear of zonal winds ( $du/dz$ ) to evaluate the Richardson number ( $R_i = N^2/(\partial u/\partial z)^2$ ), which can be used to examine the turbulence development and baroclinic stability of the atmospheric systems on the giant planets (e.g., Allison et al., 1995). Panel A of Figure 4 shows that the static stability of Saturn's atmosphere is consistently positive in the upper troposphere (i.e., 50–500 mbar), in agreement with a previous study (Fletcher et al., 2016). Positive static stability in the upper troposphere suggests that the atmosphere is convectively stable in that region. Static stability generally increases with height across all latitudes, indicating that Saturn's atmosphere becomes more stable from the 500-mbar pressure level to the tropopause (~50 mbar). Specifically, the atmospheric layers around 500 mbar exhibit a static stability approaching zero, suggesting nearly neutral stability conditions in these layers. If static stability continues to decrease with depth, it is possible that the atmospheric layers beneath the 500-mbar layer are convectively unstable. The vertical shear of zonal winds (Panel B of Figure 4) has a much larger magnitude in the equatorial region (i.e., ~20°S–20°N) than in other latitudes, consistent with the vertical structure of zonal winds shown in Panel B of Figure 2. The relatively large meridional gradients of temperature and the small values of the Coriolis parameter in the tropical region contribute to the dominant vertical shear of zonal winds in this area. Panel C of Figure 4 shows that the Richardson number is larger than three in all latitudes for Saturn's upper troposphere from 500 to 50 mbar, suggesting that turbulence is suppressed in these regions. Some areas in the tropical region from 15°S to 15°N have relatively small values of the Richardson number, implying that the equatorial region relatively favors turbulence development.

The vertical structure of zonal winds shown in Figure 2 also makes it possible to examine the meridional gradient of the zonal-mean quasi-geostrophic potential vorticity, defined as effective beta ( $\beta_e$ ). Effective beta is a critical parameter in atmospheric dynamics (Andrews et al., 1987; Holton, 2004; Pedlosky, 1987; Salby, 1996). Although this parameter has been previously analyzed in studies of Saturn's atmosphere (e.g., Fletcher et al., 2016; Li



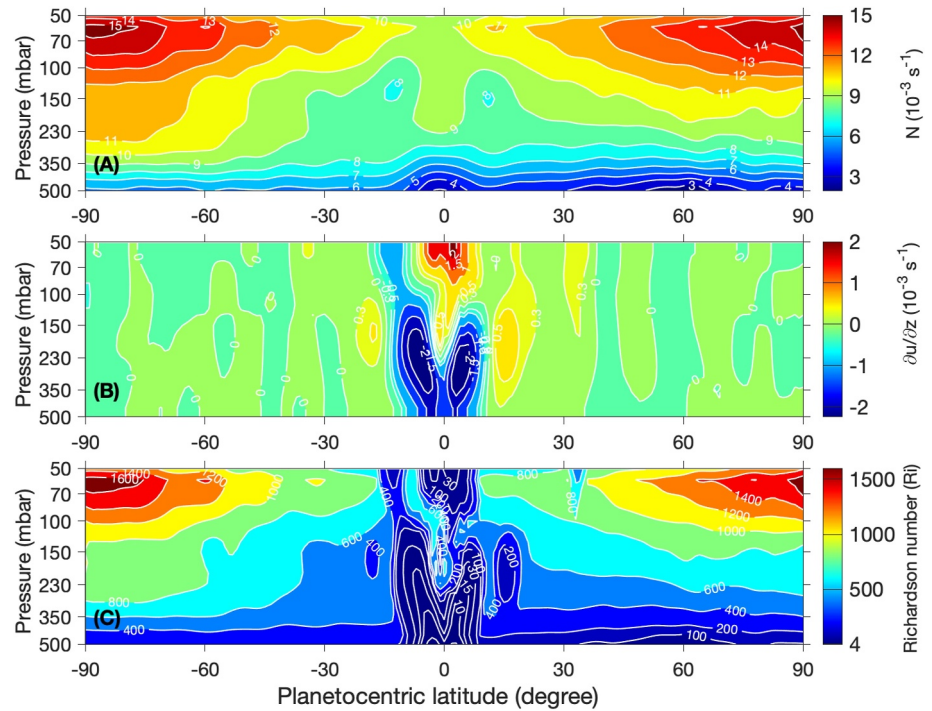


**Figure 4.** Static stability, vertical shear of zonal winds, and Richardson number. (a) Static stability ( $N$ ). (b) Vertical shear of zonal winds ( $\partial u / \partial z$ ). (c) Richardson number ( $Ri$ ).

et al., 2021; Read, Dowling, & Schubert, 2009; Read, Conrath, et al., 2009; Sánchez-Lavega et al., 2011), a complete picture of Saturn's upper troposphere, including the equatorial region, is still lacking. Effective beta can be expressed as ( $\beta_e = \beta + \beta_y + \beta_z$ ), where  $\beta$  is the meridional gradient of the planetary vorticity  $f$  (i.e., Coriolis parameter  $f = 2\Omega \sin \phi$ ),  $\beta_y$  is the meridional gradient of the zonal-average relative vorticity ( $\beta_y = -u_{yy} = -\partial^2 u / \partial y^2$ ), and  $\beta_z$  is the meridional gradient of the stretching vorticity. The last term,  $\beta_z$ , is generally expressed in the log-pressure coordinates, in which the vertical coordinate is defined as  $z^* = -H \ln(p/p_0)$ , with  $H$  as the scale height and  $p_0$  as a reference pressure (e.g., 1,000 mbar). Then, we have  $\beta_z = -(1/\rho) \partial [\rho f^2 / N^2 (\partial u / \partial z^*)] / \partial z^*$ , where  $\rho$  is atmospheric density. Effective beta can be used to examine the stability of zonal jets with a stability criterion: zonal jets are stable when  $\beta_e > 0$  and unstable when  $\beta_e < 0$ . The combination of the first two terms in  $\beta_e$  is generally used to define the stability of a barotropic atmosphere:  $\beta_b = \beta + \beta_y$ , where we define  $\beta_b$  as barotropic beta. Zonal jets in a barotropic atmosphere are stable and unstable when  $\beta_b > 0$  and  $\beta_b < 0$ , respectively. Based on the vertical structure of zonal winds derived from this study, we can calculate the aforementioned vorticity gradients and the corresponding stabilities. It is important to note that while using more precise zonal winds to examine atmospheric stability can enhance our understanding of Saturn's atmosphere, there is still a caveat. In principle, the stability theory within the framework of quasi-geostrophic potential vorticity has limitations in the equatorial region. However, in practice, the inconsistency between the quasi-geostrophic framework and the gradient wind relationship used in our thermal wind equation does not significantly impact our analysis of atmospheric stability. First, the geostrophic balance holds well even at latitudes approaching  $3^\circ$  on Saturn. Second, the most unstable conditions, associated with the westward jets, are primarily found in the middle and high latitudes.

Figure 5 displays the three components of effective beta ( $\beta_e$ ). Panel A shows that the meridional gradient of the planetary vorticity ( $f$ ) is non-negative at all latitudes: it reaches a maximal value of  $5.48 \times 10^{-12} \text{ m}^{-1} \text{ s}^{-1}$  at the equator and a minimal value of 0 at the two poles. Panel B of Figure 5 shows  $\beta_y$ , which is determined by the meridional structure of zonal winds. Comparing with the vertical structure of zonal winds shown in Figure 2, we find that there are maxima of  $\beta_y$  for these eastward jets and minima of  $\beta_y$  for these westward jets at the middle and high latitudes. For the low latitudes from  $20^\circ \text{S}$  to  $20^\circ \text{N}$ , the region between the southern peak of the equatorial jet at  $\sim 7^\circ \text{S}$  and the peak at the equator and the region between the northern peak of the equatorial jet at  $\sim 7^\circ \text{N}$  and the

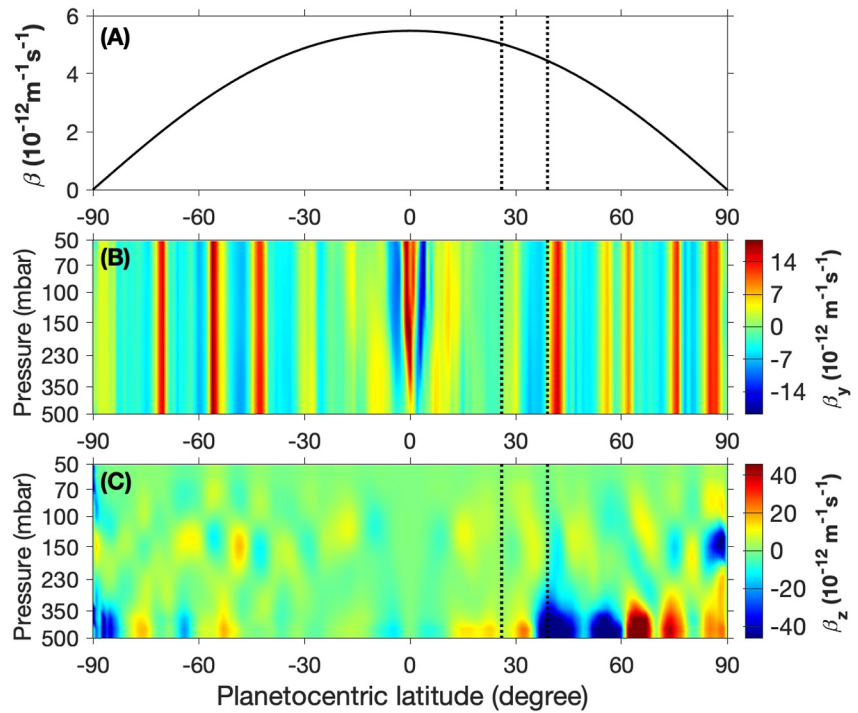


**Figure 5.** Components of effective beta. (a) The meridional gradient of the planetary vorticity ( $\beta$ ). (b) The meridional gradient of the zonally averaged relative vorticity ( $\beta_y$ ). (c) The meridional gradient of stretching vorticity ( $\beta_z$ ). The two vertical dashed lines at latitudes 26° and 39° in each panel represent the latitudinal range of the 2010 giant convective storm.

peak at the equator (i.e., the two dip structures of zonal winds around the equator) basically have negative  $\beta_y$ , while all other regions have positive  $\beta_y$ . Panel C of Figure 5 shows  $\beta_z$ , suggesting that the large magnitudes of  $\beta_z$  mainly happen in the atmospheric layers from 500 to ~300 mbar. In these layers (~300–500 mbar), Figure 5 also suggests that the magnitudes of the  $\beta_z$  (panel C) are much larger than those of  $\beta$  (panel A) and  $\beta_y$  (panel B), so  $\beta_z$  is dominant in the effective beta ( $\beta_e$ ) in such atmospheric layers.

The three components of the effective beta ( $\beta_e$ ) make it possible to examine both the barotropic and baroclinic stability criteria, which are shown in panel B and panel C of Figure 6 respectively. Panel A of Figure 6 displays the meridional structure of zonal winds at the reference, which can be used to examine the correlation between zonal winds and barotropic stability (panel B of Figure 6). Basically, barotropic beta ( $\beta_b$ ) has the same structure as that in  $\beta_y$ , because  $\beta_y$  is much larger than  $\beta$  in most latitudes especially in these latitudes around the eastward and westward jets (see Figure 5). In the middle and high latitudes, zonal winds do not significantly vary with pressure (panel B of Figure 2), so the minima and maxima of  $\beta_y$  (panel B of Figure 5) and the corresponding barotropic stability  $\beta_b$  (panel B of Figure 6), which are related to the westward and eastward jets respectively, keep constant with pressure.

For these westward jets in the middle and high latitudes, the peaks of negative  $\beta_y$  basically have magnitudes larger than those of  $\beta$ . Therefore, the barotropic stability criterion is violated ( $\beta_b < 0$ ) over these westward jets so that they are barotropically unstable, as shown in panel B of Figure 6. For the atmospheric layers from ~50 to ~200 mbar in the equatorial region, the negative peaks of  $\beta_y$  at the latitudes ~4°S and ~4°N, which corresponds to the dip structures of zonal winds on the two sides of the equator (see panel B of Figure 5), also have magnitudes larger than those of corresponding  $\beta$ . Therefore, zonal jets at 4°S and 4°N are also barotropically unstable.

As discussed in a previous study (Li, Ingersoll, & Huang, 2006), the vertical structure of zonal winds can help to stabilize the zonal jets on Jupiter and Saturn, even though zonal jets are barotropically unstable. Panel C of Figure 6 shows the baroclinic stability, which involves the vertical shear of zonal winds. This panel shows that the baroclinic stability parameter ( $\beta_e$ ) is significantly different from the barotropic stability parameter ( $\beta_b$ ) in many locations because the term involving the vertical shear of zonal winds ( $\beta_z$ ) is generally larger than the term

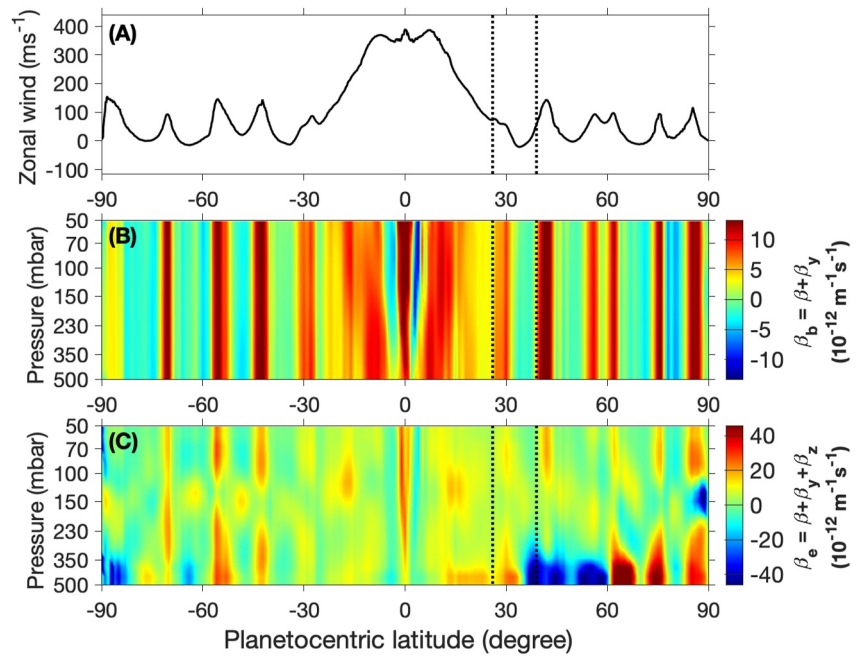


**Figure 6.** Comparison between the zonal winds and barotropic & baroclinic stabilities ( $\beta_b$  and  $\beta_e$ ). (a) The meridional profile of zonal winds at the 500-mbar pressure level. (b) The barotropic beta ( $\beta_b$ ), which is used to examine the barotropic stability of Saturn's atmosphere. (c) The effective beta ( $\beta_e$ ), which can be applied to investigate the baroclinic nature of Saturn's atmosphere. The two vertical dashed lines at latitudes 26° and 39° in each panel represent the latitudinal range of the 2010 giant convective storm.

associated to the meridional structure of zonal winds ( $\beta_y$ ). There are a series of minimum and maximum centers of  $\beta_z$  along latitude at the pressure levels around 150 mbar (panel C of Figure 5) and these centers significantly modify the barotropic stability (panel B of Figure 6) to the baroclinic stability around the pressure level of  $\sim 150$  mbar (panel C of Figure 6). There are also a series of minimum and maximum centers of  $\beta_z$  along latitude in the pressure range from  $\sim 350$  to 500 mbar (panel C of Figure 5). Additionally, these centers of  $\beta_z$  are stronger than those of  $\beta_y$  over these pressure levels (i.e.,  $\sim 350$ –500 mbar). Therefore, the term  $\beta_z$  is dominant in the baroclinic stability from  $\sim 350$  to 500 mbar (panel C of Figure 6). For the pressure range from  $\sim 350$  to 500 mbar, there is a minimum center with the strongest magnitudes of negative  $\beta_e$  for latitudes from  $\sim 40^\circ$  to  $60^\circ$  in the Northern Hemisphere. The stability analysis presented in this study (Figures 4–6) is based on the temperature and wind fields averaged over the years from 2004 to 2009, a period before the development of the 2010 giant convective storm. It is intriguing that such a minimum is adjacent to the latitudinal range of the 2010 giant convective storm, suggesting that strong baroclinic instability may have contributed to its development (Fischer et al., 2011; Fletcher, Hesman, et al., 2011; Sánchez-Lavega et al., 2011), even though deep moist convection likely played a dominant role (Li & Ingersoll, 2015; Sánchez-Lavega et al., 2011). To further explore the relationship between atmospheric stability and storm development, we examined baroclinic stability before and after the 2010 storm, as shown in Figure 7. The figure suggests that the 2010 storm modified atmospheric stability in its region by altering the thermal structure (e.g., Fletcher, Hesman, et al., 2011). At the same time, temporal variations in stability at other latitudes may be linked to seasonal temperature changes.

### 4.3. Temporal Variations of Zonal Winds

Cassini orbited Saturn from 2004 to 2017, enabling the examination of temporal variations in Saturn's zonal winds. Previous studies (García-Melendo et al., 2011; Sánchez-Lavega et al., 2016) investigated zonal wind variations from 2004–09 to 2014 at pressure levels around  $\sim 500$  and  $\sim 60$  mbar using ISS images recorded with continuum and methane-absorption filters, respectively. In this study, we also conducted zonal wind measurements based on ISS images recorded by continuum filters in 2012. A comparison of zonal winds across different years is presented in Figure 8. Panel A presents zonal winds at  $\sim 500$  mbar, suggesting relative stability during the Cassini epoch. Panel B of Figure 8 illustrates temporal variations of zonal winds at the 60-mbar pressure level

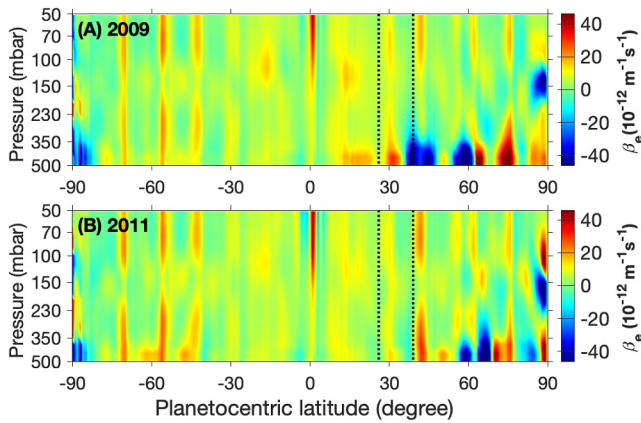


**Figure 7.** Baroclinic stability (effective beta,  $\beta_e$ ) in 2009 and 2011. (a) 2009 (pre-storm). (b) 2011 (post-storm).

(Sánchez-Lavega et al., 2016). It appears that there is a southward shift of a couple of degrees in latitude from 2004-09 to 2014 for zonal winds between latitudes  $\sim 10^\circ\text{N}$  and  $40^\circ\text{N}$ . Panel B also indicates an increase in 60-mbar zonal winds in the narrow equatorial region from  $\sim 0^\circ$  to  $5^\circ\text{N}$  between 2004-09 and 2014. Panels C and D better display the temporal variations from 2004-09 to 2014. The comparison between the two panels reveals that the temporal variations of zonal winds are much more significant at the 60-mbar pressure level than at the 500-mbar pressure level, especially in the narrow equatorial region from  $0^\circ$  to  $5^\circ\text{N}$ .

The relatively steady zonal winds at 500 mbar and unstable winds at 60 mbar are consistent with one of our previous studies based on observations in the early stage of the Cassini epoch (Li et al., 2011). The solar flux is mainly deposited around 100 mbar (Pérez-Hoyos & Sánchez-Lavega, 2006). The seasonal variations of solar flux may serve as the main driver of the temporal variations of zonal winds at 60 mbar. On the other hand, the solar flux has less influence on the relatively deep atmosphere around 500 mbar, which can help

explain the relatively stable zonal winds there. Panel B of Figure 5 suggests that the negative  $\beta_y$  at  $\sim 4^\circ\text{N}$  and 50-mbar has the largest magnitude compared to those at other locations, implying that the equatorial zonal jets around  $4^\circ\text{N}$  and 50 mbar are the most unstable. This finding can also contribute to the significant temporal variations of the 60-mbar equatorial jets revealed by the ISS observations (panel B of Figure 8).

The ISS measurements of zonal winds in 2004-09 and 2014 at the level of 60 mbar, which are shown in Figure 8, enable the examination of temporal variations in zonal winds computed from the CIRS-retrieved temperature using the thermal-wind relationship. Figure 9 shows the comparison of the temporal variations of the 60-mbar zonal winds between the ISS cloud-tracking measurements (panel A) and the computed zonal winds from the

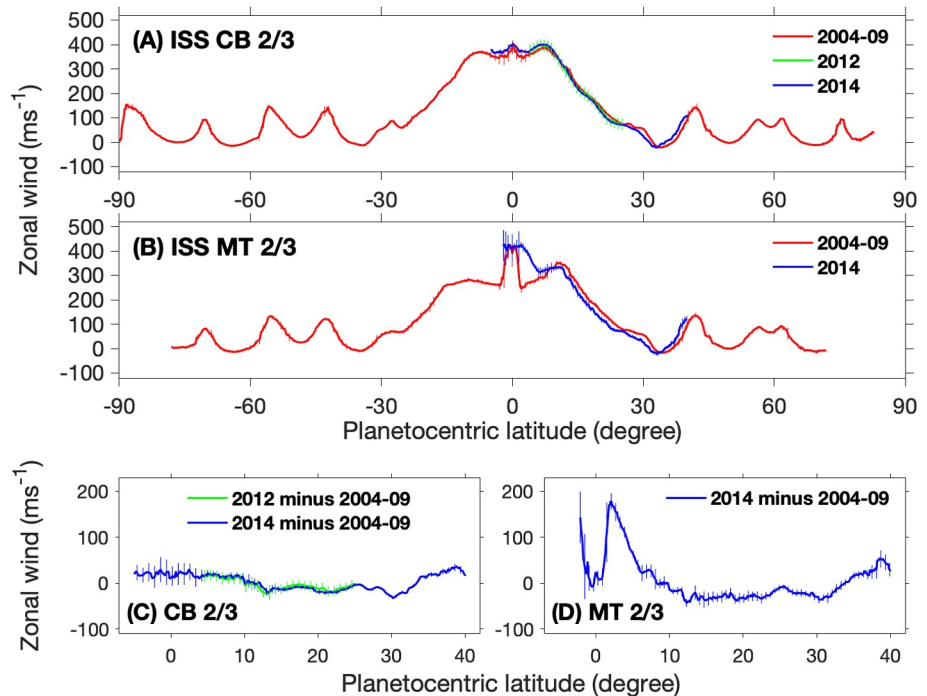


**Figure 8.** Temporal variations of zonal winds on Saturn. (a) Measurements of zonal winds at the levels of the top visible clouds ( $\sim 500$  mbar) in different years. (b) Measurements of zonal winds around the tropopause ( $\sim 60$  mbar). (c) Temporal variations of zonal winds based on panel (a). (d) Temporal variations of zonal winds based on panel (b). The measurements are based on the Cassini ISS continuum (panels a, c) and methane-absorption (panels b, d) filters. The subsolar latitude has moved to the northern hemisphere since 2009, so Saturn's northern hemisphere has been well recorded by the Cassini ISS since then.



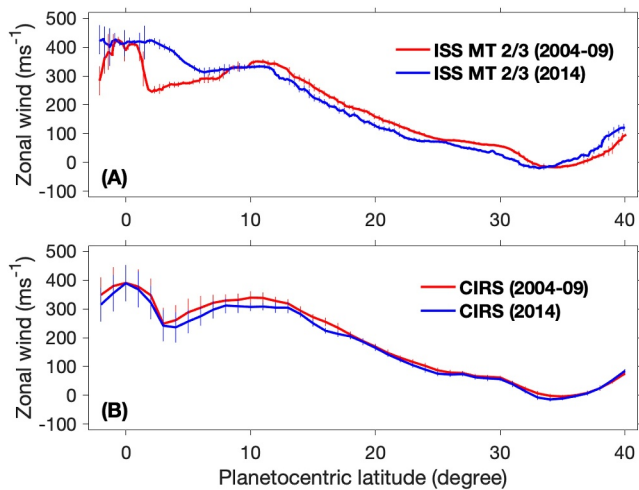


**Figure 9.** Comparison of 60-mbar zonal winds between the ISS measurements and the CIRS computations. (a) The ISS-measured zonal winds around 60 mbar in different years. (b) The CIRS-computed zonal winds at the same level (60 mbar) in different years.

(i.e., 2006, 2009, 2011, and 2015) during the Cassini epoch (2004–2017). Once we selected suitable image pairs, we processed them into maps that could be directly used for wind measurements.

Figure 10 presents the results of our wind measurements. The solid line in panel A comes from our previous study (Studwell et al., 2018), and the colorful dots represent the new measurements by tracking discrete cloud features. In panel B, we averaged the new measurements over latitude bins with a width of  $1^\circ$ . This figure shows that most of the temporal variations in the tropical winds are smaller than the uncertainties in the wind measurements, leading us to conclude that the temporal variations of the zonal winds around 2,000 mbar are not statistically significant. This finding further suggests that Saturn's relatively deep atmospheric layers around 2,000 mbar do not experience significant temporal variations in the tropical region.

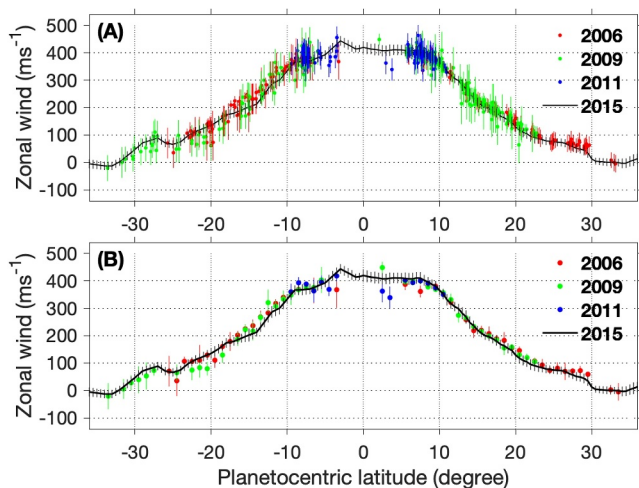


**Figure 10.** Zonal winds in Saturn's relatively deep atmosphere ( $\sim 2,000$  mbar) based on images recorded at  $5 \mu\text{m}$  by the Cassini/VIMS over multiple years. (a) Raw measurements. (b) Binned results. The raw measurements in panel (a) are averaged over a  $1^\circ$ -degree bin in latitude to obtain the averaged zonal winds, which is shown in panel (b). Zonal winds in 2015 are from a previous study (Studwell et al., 2018).

CIRS temperature (panel B). Panel B reveals relatively small variations in the computed zonal winds from 2004 to 09 to 2014. The temporal variations are smaller than the uncertainties of computed zonal winds, suggesting that the changes are not statistically significant. The temporal variations of the computed zonal winds (panel B) do not align with the temporal variations of the ISS-measured zonal winds (panel A), especially for the narrow equatorial zone from  $\sim 2^\circ\text{S}$  to  $5^\circ\text{N}$ . The physics behind the inconsistency in temporal variations between ISS-measured winds and CIRS-computed winds is unclear. There is uncertainty in estimating the pressure level of the ISS winds (60 mbar) (García-Melendo et al., 2010, 2011; Sanchez-Lavega et al., 2016), which possibly contributes to the aforementioned inconsistency.

We also examine the temporal variations of zonal winds in the relatively deep atmosphere around 2,000 mbar, probed by the VIMS  $5\text{-}\mu\text{m}$  images. Here, we focus on the tropical region from  $35^\circ\text{S}$  to  $35^\circ\text{N}$  because the significant temporal variations at the relatively shallow layers (i.e., 500 and 50 mbar) explored by the ISS images mainly occur in this region. Selecting the VIMS image pairs for wind measurements involved strict requirements such as necessary spatial resolution, suitable time separation, and adequate overlap in the longitude direction between a pair of images. While searching the public VIMS database, we only found high-quality image pairs for specific years

The VIMS winds around the 2,000-mbar level are further compared to the ISS winds around the 500-mbar level, as shown in Figure 11. The VIMS winds are stronger than the ISS winds within a narrow latitude band from  $5^\circ\text{S}$  to  $5^\circ\text{N}$ , suggesting that the equatorial winds become stronger when going deeper in that region. This finding is consistent with a previous study (Studwell et al., 2018). The thermal-wind investigation based on the CIRS temperature (Figure 2) shows that the vertical shear of zonal winds in such a narrow latitude band ( $5^\circ\text{S}$ – $5^\circ\text{N}$ ) is negative around 500 mbar, suggesting that the equatorial winds decrease with altitude and hence increase with depth around the 500-mbar pressure level. Assuming that the vertical shear of zonal winds remains constant from 500 to 2,000 mbar, we can estimate the extrapolated zonal winds at the 2,000-mbar pressure. Figure 11 also shows the comparison between the extrapolated zonal winds and the VIMS-measured zonal winds, which reveals that the extrapolated zonal winds are stronger than the VIMS-measured zonal winds. The thermal wind relationship suggests that the vertical shear of zonal winds is proportional to the meridional gradient of temperature; therefore, the comparison presented in Figure 11 implies that the average meridional gradients of temperature in the pressure range from 500 to 2,000 mbar are smaller than the CIRS-observed temperature gradients at the 500-mbar pressure level for the narrow latitude band from  $5^\circ\text{S}$  to  $5^\circ\text{N}$ . The differential solar flux is probably the main driver of the meridional gradient of atmospheric temperature. The influence of solar flux on the atmospheric structure is weaker for pressure levels deeper than the 500-mbar level compared to pressure levels shallower than the 500-mbar level (Pérez-Hoyos



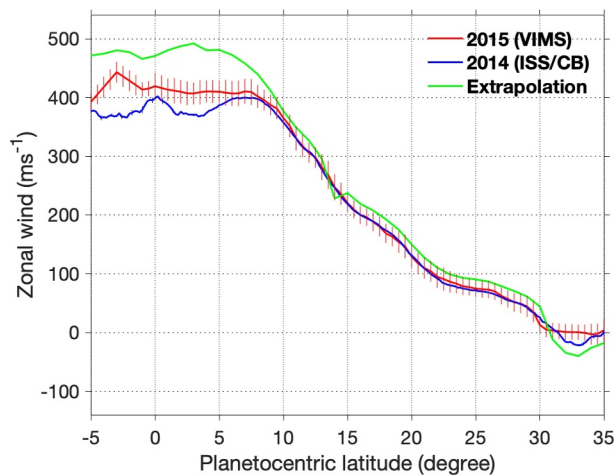


**Figure 11.** Comparison between the 2000-mbar zonal winds measured by the VIMS and the 500-mbar zonal winds measured by the ISS. There are no ISS wind measurements corresponding to the time of the VIMS winds (2015), so we selected the ISS measurements closest in time (2014). The extrapolated zonal winds at the 2000-mbar level, estimated from the vertical shear of zonal winds at 500-mbar from the CIRS temperature, are also included in the figure for comparison.

& Sánchez-Lavega, 2006), which can explain the relatively weak meridional gradients of temperature for the pressures from 500 to 2,000 mbar compared to those around 500 mbar. It is also possible that the uncertainty in estimating the pressure levels of the zonal winds based on the ISS and VIMS images may contribute to the discrepancy between the extrapolated zonal winds and the VIMS-measured zonal winds.

## 5. Summary and Discussion

A thermal-wind equation, which is more general than the classic thermal-wind equation, has been developed in recent studies (de la Torre Juárez et al., 2002; Flasar, Achterberg, Conrath, Gierasch, et al., 2005; Flasar, Achterberg, Conrath, Pearl, et al., 2005b; Fouchet et al., 2008; Galanti et al., 2017; Li et al., 2007, 2008; Marcus et al., 2019). The general equation, not dependent on geostrophic balance, can be applied at all latitudes, including the equatorial region. However, the equation has an integration gap in the equatorial region, caused by its cylindrical integration path, introducing limitations in investigating the equatorial winds. In this study, we develop an algorithm to address this limitation so that zonal winds in the equatorial region can be fully investigated. The comparison between the computed equatorial winds using the algorithm and Cassini-measured winds shows qualitative consistency, validating the algorithm.

The algorithm is applied to Cassini observations to derive a complete picture of the vertical structure of zonal winds at all latitudes, including the equatorial region. In the middle and high latitudes, zonal winds do not significantly vary with altitude, consistent with previous studies (e.g., Fletcher et al., 2016; Read, Conrath, et al., 2009). In the low latitudes, the vertical structure of the equatorial zonal winds from 10°S to 10°N displays complicated structures: the zonal winds initially decrease with altitude and then increase. In particular, the equatorial jet between 3°S and 3°N extends throughout the entire pressure range of 50–500 mbar and widens with altitude. The complete picture of zonal winds is further used to investigate atmospheric stability, suggesting strong instability from latitudes ~40°N to ~60°N, around the pressure range of 350–500 mbar, mainly caused by atmospheric baroclinicity. This latitude range is related to the latitude range of the 2010 giant storm, suggesting that baroclinic instability may also play a role in the development of the upper layer of the storm. In the equatorial region, a narrow strong jet between 3°S and 3°N generates dip structures of zonal winds on both sides of the equator, resulting in barotropic instability in these regions, increasing in strength from the 500-mbar level to the 50-mbar level.

Cassini long-term multi-instrument observations are also used to examine the temporal variations of zonal winds in the equatorial region. While the equatorial zonal winds at 500 mbar display temporal stability, the equatorial zonal winds from 0° to 5°N at 60 mbar exhibit significant temporal variations. Seasonally varying solar flux is one of the drivers of the temporal variations of zonal winds at the pressure levels around 60 mbar. Some dynamic processes, such as eddies/vortices, storms, and waves/oscillations, may also contribute to the temporal variations of zonal winds in Saturn's atmospheric layers around the tropopause. Furthermore, stability analysis suggests that the strongest barotropic instability in the equatorial region mainly occurs around the 60-mbar level, which probably contributes to the significant temporal variations at high altitudes too. For the temporal stability of zonal winds around 500 mbar, there are two factors. First, solar flux deposition and its seasonal variation primarily occur in the atmospheric layers around 100 mbar, rather than those around 500 mbar (Pérez-Hoyos & Sánchez-Lavega, 2006), which may help explain the stability at 500 mbar. Second, the longer radiative time constant of the atmospheric layers around 500 mbar, compared to that of the layers around 60 mbar, also contributes to the stability observed at 500 mbar.

The spatio-temporal characteristics of zonal winds revealed by this study can aid scientists in understanding equatorial dynamics (e.g., equatorial oscillations, as discussed in Fouchet et al., 2008; Orton et al., 2008) and enhance numerical models by providing essential observational constraints. Investigations based on the recent observations of Saturn from the James Webb Space Telescope can help us continue monitoring the temporal variations of Saturn's atmospheric dynamics in the post-Cassini era (Fletcher et al., 2023). The algorithm

developed to fill equatorial gaps caused by integration routines of the general thermal-wind equation can help not only explore Saturn's zonal winds and atmospheric dynamics but also has potential applications in the exploration of other giant planets. A recent analysis reveals an intense equatorial jet confined to  $\pm 3^\circ$  in latitude on Jupiter (Hueso et al., 2023). It will be interesting to explore the vertical structure of this narrow equatorial jet using new thermal observations and the general thermal wind equation with the algorithm.

## Data Availability Statement

The Cassini raw data used in this study are publicly available through NASA's Planetary Data System: Composite Infrared Spectrometer (CIRS) (Showalter & Gordon, 2011), Imaging Science Subsystem (ISS) (Porco & Cassini Imaging Science Team, 2020), and Visual and Infrared Mapping Spectrometer (VIMS) (Brown & VIMS Science Team, 2020). The processed data and the code used to calculate Saturn's zonal winds via the general thermal wind equation are available at Wang (2024).

## Acknowledgments

We are grateful to the Cassini CIRS, ISS, and VIMS teams for recording the raw data sets. Liming Li acknowledges the support received from the NASA ROSES Cassini Data Analysis Program and the NSF Astronomy and Astrophysics Research Program. Leigh N. Fletcher was supported by a European Research Council Consolidator Grant (under the European Union's Horizon 2020 research and innovation programme, Grant 723890) at the University of Leicester. Agustín Sánchez-Lavega and Ricardo Hueso were supported by Grant PID2019-109467GB-I00 funded by MCIN/AEI/10.13039/501100011033/and by Grupos Gobierno Vasco IT1742-22.

## References

- Allison, M., Del Genio, A. D., & Zhou, W. (1995). Richardson number constraints for the Jupiter and outer planet wind regime. *Geophysical Research Letters*, 22(21), 2957–2960. <https://doi.org/10.1029/95gl02818>
- Anderson, J. D., & Schubert, G. (2007). Saturn's gravitational field, internal rotation, and interior structure. *Science*, 317(5843), 1384–1387. <https://doi.org/10.1126/science.1144835>
- Andrews, D. G., Holton, J. R., & Leovy, C. B. (1987). *Middle atmosphere dynamics*. Academic Press.
- Archinal, B. A., Acton, C. H., A'Hearn, M. F., Conrad, A., Consolmagno, G. J., Duxbury, T., et al. (2018). Report of the IAU working group on cartographic coordinates and rotational elements: 2015. *Celestial Mechanics and Dynamical Astronomy*, 130(3), 1–46. <https://doi.org/10.1007/s10569-017-9805-5>
- Baines, K. H., Momary, T. W., Fletcher, L. N., Showman, A. P., Roos-Serote, M., Brown, R. H., et al. (2009). Saturn's north polar cyclone and hexagon at depth revealed by Cassini/VIMS. *Planetary and Space Science*, 57(14–15), 1671–1681. <https://doi.org/10.1016/j.pss.2009.06.026>
- Baines, K. H., Momary, T. W., & Roos-Serote, M. (2005). The deep winds of Saturn: First measurements of the zonal windfield near the two-bar level. *Bulletin of the American Astronomical Society*, 37, 658.
- Batchelor, G. K. (1967). *An introduction to fluid dynamics*. Cambridge University Press.
- Bevington, P. R., & Robinson, D. K. (2003). *Data reduction and error analysis for the physical sciences* (3rd ed.). McGraw-Hill.
- Brown, R. H., & VIMS Science Team. (2020). VIMS observations from the Cassini tour of the Saturn system. NASA Planetary Data System, urn:nasa:pds:cassini\_vims\_saturn::1.0. <https://doi.org/10.17189/1504134>
- Brown, R. H., Baines, K. H., Bellucci, G., Bibring, J. P., Buratti, B. J., Capaccioni, F., et al. (2004). The Cassini visual and infrared mapping spectrometer (VIMS) investigation. *Space Science Reviews*, 115(1–4), 111–168. <https://doi.org/10.1007/s11214-004-1453-x>
- Choi, D. S., Showman, A. P., & Brown, R. H. (2009). Cloud features and zonal wind measurements of Saturn's atmosphere as observed by Cassini/VIMS. *Journal of Geophysical Research*, 114(E4). <https://doi.org/10.1029/2008je003254>
- Conrath, B. J., & Gautier, D. (1980). Thermal structure of Jupiter's atmosphere obtained by inversion of Voyager 1 infrared measurements. *Remote Sensing of Atmospheres and Oceans*, 611–628.
- Conrath, B. J., Gierasch, P. J., & Ustinov, E. A. (1998). Thermal structure and para hydrogen fraction on the outer planets from Voyager IRIS measurements. *Icarus*, 135(2), 501–517. <https://doi.org/10.1006/icar.1998.6000>
- de Latorre Juárez, M., Fisher, B. M., & Orton, G. S. (2002). Large scale geostrophic winds with a full representation of the Coriolis force: Application to IR observations of the upper Jovian troposphere. *Geophysical & Astrophysical Fluid Dynamics*, 96(2), 87–114. <https://doi.org/10.1080/03091920290027943>
- Del Genio, A. D., Achterberg, R. K., Baines, K. H., Flasar, F. M., Read, P. L., Sánchez-Lavega, A., & Showman, A. P. (2009). Saturn atmospheric structure and dynamics. *Saturn from Cassini-Huygens*, 113–159. [https://doi.org/10.1007/978-1-4020-9217-6\\_6](https://doi.org/10.1007/978-1-4020-9217-6_6)
- Desch, M. D., & Kaiser, M. L. (1981). Voyager measurement of the rotation period of Saturn's magnetic-field. *Geophysical Research Letters*, 83(3), 253–256. <https://doi.org/10.1029/gl008i003p00253>
- Fischer, G., Kurth, W. S., Gurnett, D. A., Zarka, P., Dyudina, U. A., Ingersoll, A. P., et al. (2011). A giant thunderstorm on Saturn. *Nature*, 475(7354), 75–77. <https://doi.org/10.1038/nature10205>
- Flasar, F. M., Achterberg, R. K., Conrath, B. J., Gierasch, P. J., Kunde, V. G., Nixon, C. A., et al. (2005a). Titan's atmospheric temperatures, winds, and composition. *Science*, 308(5724), 975–978. <https://doi.org/10.1126/science.1111150>
- Flasar, F. M., Achterberg, R. K., Conrath, B. J., Pearl, J. C., Bjoraker, G. L., Jennings, D. E., et al. (2005b). Temperatures, winds, and composition in the Saturnian system. *Science*, 307(5713), 1247–1251. <https://doi.org/10.1126/science.1105806>
- Flasar, F. M., Kunde, V. G., Abbas, M. M., Achterberg, R. K., Ade, P., Barucci, A., et al. (2004). Exploring the Saturn system in the thermal infrared: The composite infrared spectrometer. *Space Science Reviews*, 115, 169–297. [https://doi.org/10.1007/1-4020-3874-7\\_4](https://doi.org/10.1007/1-4020-3874-7_4)
- Fletcher, L. N., Baines, K. H., Momary, T. W., Showman, A. P., Irwin, P. G., Orton, G. S., et al. (2011). Saturn's tropospheric composition and clouds from Cassini/VIMS 4.6–5.1  $\mu\text{m}$  nightside spectroscopy. *Icarus*, 214(2), 510–533. <https://doi.org/10.1016/j.icarus.2011.06.006>
- Fletcher, L. N., Greathouse, T. K., Guerlet, S., Moses, J. I., & West, R. A. (2018). Saturn's temporally changing atmosphere. *Saturn in the 21st Century*, 20, 251–294.
- Fletcher, L. N., Guerlet, S., Orton, G. S., Cosentino, R. G., Fouchet, T., Irwin, P. G., et al. (2017). Disruption of Saturn's quasi-periodic equatorial oscillation by the great northern storm. *Nature Astronomy*, 1(11), 765–770. <https://doi.org/10.1038/s41550-017-0271-5>
- Fletcher, L. N., Hesman, B. E., Irwin, P. G. J., Baines, K. H., Momary, T. W., Sanchez-Lavega, A., et al. (2011). Thermal structure and dynamics of Saturn's northern springtime disturbance. *Science*, 332(6036), 1413–1417. <https://doi.org/10.1126/science.1204774>
- Fletcher, L. N., Irwin, P. G., Achterberg, R. K., Orton, G. S., & Flasar, F. M. (2016). Seasonal variability of Saturn's tropospheric temperatures, winds and para-H<sub>2</sub> from Cassini far-IR spectroscopy. *Icarus*, 264, 137–159. <https://doi.org/10.1016/j.icarus.2015.09.009>
- Fletcher, L. N., Irwin, P. G. J., Teanby, N. A., Orton, G. S., Parrish, P. D., de Kok, R., et al. (2007). Characterising Saturn's vertical temperature structure from Cassini/CIRS. *Icarus*, 189(2), 457–478. <https://doi.org/10.1016/j.icarus.2007.02.006>

- Fletcher, L. N., King, O. R., Harkett, J., Hammel, H. B., Roman, M. T., Melin, H., et al. (2023). Saturn's atmosphere in northern summer revealed by JWST/MIRI. *Journal of Geophysical Research: Planets*, 128(9), e2023JE007924. <https://doi.org/10.1029/2023je007924>
- Fouchet, T., Guerlet, S., Strobel, D. F., Simon-Miller, A. A., Bézard, B., & Flasar, F. M. (2008). An equatorial oscillation in Saturn's middle atmosphere. *Nature*, 453(7192), 200–202. <https://doi.org/10.1038/nature06912>
- Gaddis, L., Anderson, J., Becker, K., Becker, T., Cook, D., Edwards, K., et al. (1997). An overview of the integrated software for imaging spectrometers (ISIS). *Lunar and Planetary Science Conference*, 28, 387.
- Galanti, E., Kaspi, Y., & Tziperman, E. (2017). A full, self-consistent treatment of thermal wind balance on oblate fluid planets. *Journal of Fluid Mechanics*, 810, 175–195. <https://doi.org/10.1017/jfm.2016.687>
- García-Melendo, E., Pérez-Hoyos, S., Sánchez-Lavega, A., & Hueso, R. (2011). Saturn's zonal wind profile in 2004–2009 from Cassini ISS images and its long-term variability. *Icarus*, 215(1), 62–74. <https://doi.org/10.1016/j.icarus.2011.07.005>
- García-Melendo, E., Sánchez-Lavega, A., Legarreta, J., Perez-Hoyos, S., & Hueso, R. (2010). A strong high altitude narrow jet detected at Saturn's equator. *Geophysical Research Letters*, 37(22). <https://doi.org/10.1029/2010gl045434>
- García-Melendo, E., & Sánchez-Lavega, A. (2001). *Icarus*, 152(2), 316–330.
- Giamperi, G., Dougherty, M. K., Smith, E. J., & Russell, C. T. (2006). A regular period for Saturn's magnetic field that may track its internal rotation. *Nature*, 441(7089), 62–64. <https://doi.org/10.1038/nature04750>
- Helled, R., Galanti, E., & Kaspi, Y. (2015). Saturn's fast spin determined from its gravitational field and oblateness. *Nature*, 520(7546), 202–204. <https://doi.org/10.1038/nature14278>
- Helled, R., Schubert, G., & Anderson, J. D. (2009). Jupiter and Saturn rotation periods. *Planetary and Space Science*, 57(12), 1467–1473. <https://doi.org/10.1016/j.pss.2009.07.008>
- Holton, J. R. (2004). *An introduction to dynamic meteorology* (4th ed.). Academic Press.
- Hueso, R., Sánchez-Lavega, A., Fouchet, T., de Pater, I., Antuñano, A., Fletcher, L. N., et al. (2023). An intense narrow equatorial jet in Jupiter's lower stratosphere observed by JWST. *Nature Astronomy*, 7(12), 1454–1462. <https://doi.org/10.1038/s41550-023-02099-2>
- Ingersoll, A. P. (2020). Cassini exploration of the planet Saturn: A comprehensive review. *Space Science Reviews*, 216(8), 122–172. <https://doi.org/10.1007/s11214-020-00751-1>
- Li, C., & Ingersoll, A. (2015). Moist convection in hydrogen atmospheres and the frequency of Saturn's giant storms. *Nature Geoscience*, 8(5), 398–403. <https://doi.org/10.1038/ngeo2405>
- Li, L., Achterberg, R. K., Conrath, B. J., Gierasch, P. J., Smith, M. A., Simon-Miller, A. A., et al. (2013). Strong temporal variability over one Saturnian year: From Voyager to Cassini. *Scientific Reports*, 3(1), 2410. <https://doi.org/10.1038/srep02410>
- Li, L., Conrath, B. J., Flasar, F. M., & Gierasch, P. J. (2007). Revisit of the thermal wind equation: Application to planetary atmospheres at low latitudes. *EOS Transactions American Geophysical Union*, 88(24), P41A–P0208.
- Li, L., Gierasch, P. J., Achterberg, R. K., Conrath, B. J., Flasar, F. M., Vasavada, A. R., et al. (2008). Strong jet and a new thermal wave in Saturn's equatorial stratosphere. *Geophysical Research Letters*, 35(23). <https://doi.org/10.1029/2008gl035515>
- Li, L., Ingersoll, A. P., & Huang, X. L. (2006). Interaction of moist convection with zonal jets on Jupiter and Saturn. *Icarus*, 180(1), 113–123. <https://doi.org/10.1016/j.icarus.2005.08.016>
- Li, L., Ingersoll, A. P., Vasavada, A. R., Porco, C. C., Del Genio, A. D., & Ewald, S. P. (2004). Life cycles of spots on Jupiter from Cassini images. *Icarus*, 172(1), 9–23. <https://doi.org/10.1016/j.icarus.2003.10.015>
- Li, L., Ingersoll, A. P., Vasavada, A. R., Simon-Miller, A. A., Del Genio, A. D., Ewald, S. P., et al. (2006a). Vertical wind shear on Jupiter from Cassini images. *Journal of Geophysical Research*, 111(E4), E04004. <https://doi.org/10.1029/2005je002556>
- Li, L., Jiang, X., Ingersoll, A. P., Del Genio, A. D., Porco, C. C., West, R. A., et al. (2011). Equatorial winds on Saturn and the stratospheric oscillation. *Nature Geoscience*, 4(11), 750–752. <https://doi.org/10.1038/ngeo1292>
- Li, L., Studwell, A., Dowling, T. E., Bradley, M. E., Creecy, E. C., Albright, R. J., & Jiang, X. (2021). Unsymmetrical expansion of bright clouds from Saturn's 2010 great white storm. *Icarus*, 369, 114650. <https://doi.org/10.1016/j.icarus.2021.114650>
- Limaye, S. S. (1986). Jupiter: New estimates of the mean zonal flow at the cloud level. *Icarus*, 65(2–3), 335–352. [https://doi.org/10.1016/0019-1035\(86\)90142-9](https://doi.org/10.1016/0019-1035(86)90142-9)
- Mankovich, C., Marley, M. S., Fortney, J. J., & Movshovitz, N. (2019). Cassini ring seismology as a probe of Saturn's interior. I. Rigid rotation. *The Astrophysical Journal*, 871, 1. <https://doi.org/10.3847/1538-4357/aaf798>
- Marcus, P. S., Tollefson, J., Wong, M. H., & de Pater, I. (2019). An equatorial thermal wind equation: Applications to Jupiter. *Icarus*, 324, 198–223. <https://doi.org/10.1016/j.icarus.2018.09.037>
- McCord, T. B., Coradini, A., Hibbitts, C., Capaccioni, F., Hansen, G., Filacchione, G., et al. (2004). Cassini VIMS observations of the Galilean satellites including the VIMS calibration procedure. *Icarus*, 172(1), 104–126. <https://doi.org/10.1016/j.icarus.2004.07.001>
- Militzer, B., & Hubbard, W. B. (2023). Relation of gravity, winds, and the moment of inertia of Jupiter and Saturn. *The Planetary Science Journal*, 4(5), 95. <https://doi.org/10.3847/psj/acd2cd>
- Momary, T. W., & Baines, K. H., & Cassini/VIMS Science Team. (2006). The zoology of Saturn: The bizarre features unveiled by the 5 micron eyes of Cassini/VIMS. *AAS/Division for Planetary Sciences Meeting Abstracts*, 38, 11–21.
- Orton, G. S., Yanamandra-Fisher, P. A., Fisher, B. M., Friedson, A. J., Parrish, P. D., Nelson, J. F., et al. (2008). Semi-annual oscillations in Saturn's low-latitude stratospheric temperatures. *Nature*, 453(7192), 196–199. <https://doi.org/10.1038/nature06897>
- Pedlosky, J. (1987). *Geophysical fluid dynamics*. Springer-Verlag Press.
- Pérez-Hoyos, S., & Sánchez-Lavega, A. (2006). Solar flux in Saturn's atmosphere: Penetration and heating rates in the aerosol and cloud layers. *Icarus*, 180(2), 368–378. <https://doi.org/10.1016/j.icarus.2005.10.009>
- Porco, C. C., & Cassini Imaging Science Team. (2020). ISS observations from the Cassini tour of the Saturn system. NASA Planetary Data System, urn:nasa:pds:cassini\_iss\_saturn::1.0. <https://doi.org/10.17189/1504133>
- Porco, C. C., Baker, E., Barbara, J., Beurle, K., Brahic, A., Burns, J. A., et al. (2005). Cassini imaging science: Initial results on Saturn's atmosphere. *Science*, 307(5713), 1243–1247. <https://doi.org/10.1126/science.1107691>
- Porco, C. C., West, R. A., Squyres, S., McEwen, A., Thomas, P., Murray, C. D., et al. (2004). Cassini imaging science: Instrument characteristics and anticipated scientific investigations at Saturn. *Space Science Reviews*, 115(1–4), 363–497. <https://doi.org/10.1007/s11214-004-1456-7>
- Read, P. L., Conrath, B., Fletcher, L., Gierasch, P., Simon-Miller, A., & Zuchowski, L. (2009). Mapping potential vorticity dynamics on Saturn: Zonal mean circulation from Cassini and Voyager data. *Planetary and Space Science*, 57(14–15), 1682–1698. <https://doi.org/10.1016/j.pss.2009.03.004>
- Read, P. L., Dowling, T. E., & Schubert, G. (2009). Saturn's rotation period from its atmospheric planetary-wave configuration. *Nature*, 460(7255), 608–610. <https://doi.org/10.1038/nature08194>
- Salby, M. L. (1996). *Fundamentals of atmospheric physics*. Academic Press.

- Sánchez-Lavega, A., García-Melendo, E., Pérez-Hoyos, S., Hueso, R., Wong, M. H., Simon, A., et al. (2016). An enduring rapidly moving storm as a guide to Saturn's Equatorial jet's complex structure. *Nature Communications*, 7(1), 13262. <https://doi.org/10.1038/ncomms13262>
- Sánchez-Lavega, A., Irwin, P., & García-Muñoz, A. (2023). Dynamics and clouds in planetary atmospheres from telescopic observations. *Astronomy and Astrophysics Review*, 31(1), 5. <https://doi.org/10.1007/s00159-023-00150-9>
- Sánchez-Lavega, A., Río-Gaztelurrutia, T. d., Hueso, R., Gómez-Forrellad, J. M., Sanz-Requena, J. F., Legarreta, J., et al. (2011). Deep winds beneath Saturn's upper clouds from a temporal long-lived planetary-scale storm. *Nature*, 475(7354), 71–74. <https://doi.org/10.1038/nature10203>
- Sánchez-Lavega, A., Rojas, J. F., & Sada, P. V. (2000). Saturn's zonal winds at cloud level. *Icarus*, 147(2), 405–420. <https://doi.org/10.1006/icar.2000.6449>
- Sayanagi, K. M., Dyudina, U. A., Ewald, S. P., Fischer, G., Ingersoll, A. P., Kurth, W. S., et al. (2013). Dynamics of Saturn's great storm of 2010–2011 from Cassini ISS and RPWS. *Icarus*, 223(1), 460–478. <https://doi.org/10.1016/j.icarus.2012.12.013>
- Showalter, M. R., & Gordon, M. K. (2011). Cassini Saturn composite infrared spectrometer reformatted data, NASA planetary data system, CO-S-CIRS-2/3/4-REFORMATTED-V1.0. <https://doi.org/10.17189/1519389>
- Sromovsky, L. A., & Fry, P. M. (2010). The source of widespread 3-μm absorption in Jupiter's clouds: Constraints from 2000 Cassini VIMS observations. *Icarus*, 210(1), 230–257. <https://doi.org/10.1016/j.icarus.2010.06.039>
- Studwell, A., Li, L., Jiang, X., Baines, K. H., Fry, P. M., Momary, T. W., & Dyudina, U. A. (2018). Saturn's global zonal winds explored by Cassini/VIMS 5-μm images. *Geophysical Research Letters*, 45(14), 6823–6831. <https://doi.org/10.1029/2018gl078139>
- Sun, Z. P., Stoker, C. R., & Schubert, G. (1991). Thermal and humidity winds in outer planet atmospheres. *Icarus*, 91(1), 154–160. [https://doi.org/10.1016/0019-1035\(91\)90134-f](https://doi.org/10.1016/0019-1035(91)90134-f)
- Tollefson, J., De Pater, I., Molter, E. M., Sault, R. J., Butler, B. J., Luszcz-Cook, S., & DeBoer, D. (2021). Neptune's spatial brightness temperature variations from the VLA and Alma. *The Planetary Science Journal*, 2(3), 105. <https://doi.org/10.3847/PSJ/abf837>
- Vasavada, A. R., Hörst, S. M., Kennedy, M. R., Ingersoll, A. P., Porco, C. C., Del Genio, A. D., & West, R. A. (2006). Cassini imaging of Saturn: Southern hemisphere winds and vortices. *Journal of Geophysical Research*, 111(E5). <https://doi.org/10.1029/2005je002563>
- Wang, X. (2024). Spatiotemporal variability of Saturn's zonal winds observed by Cassini [Dataset]. *Zenodo*. <https://doi.org/10.5281/zenodo.13924507>